Title:

Electrochemical Dy-Alloy Behaviors of Ni-Based Alloys in Molten LiF–CaF_2–DyF_3 and LiCl–KCl: Effects of Temperature and Electrolysis Potential

Authors:

Kouji Yasuda[1, 2,*1], Tetsuo Oishi[3], Tomomi Kagotani[4], Kenji Kawaguchi[4], Miki Yaguchi[3], Terumichi Enomoto[2,4], and Toshiyuki Nohira[4,*]

Affiliation:

[1]Agency for Health, Safety and Environment, Kyoto University, Yoshida-honmachi, Sakyo-ku, Kyoto 606-8501, Japan

[2]Department of Fundamental Energy Science, Graduate School of Energy Science, Kyoto University, Yoshida-honmachi, Sakyo-ku, Kyoto 606-8501, Japan

[3]National Institute of Advanced Industrial Science and Technology (AIST), Tsukuba, Ibaraki 305-8569, Japan

[4]Institute of Advanced Energy, Kyoto University, Gokasho, Uji, Kyoto 611-0011, Japan

[*1]Present Address: Department of Materials Science and Engineering, Graduate School of Engineering, Kyoto University, Yoshida-honmachi, Sakyo-ku, Kyoto 606-8501, Japan

*** Corresponding authors, E-mail:**

yasuda.kouji.3v@kyoto-u.ac.jp (K. Yasuda)

nohira.toshiyuki.8r@kyoto-u.ac.jp (T. Nohira)

Abstract

The effects of temperature and electrolysis potential on the alloying rate, structure, and mechanical strength for the Dy-alloyed Hastelloy C-276 samples, where Hastelloy C-276 is a Ni-based alloy containing Cr and Mo, were investigated in a molten LiF–CaF_2–DyF_3 (0.30 or 0.50 mol%) system at 1123–1323 K and a molten LiCl–KCl–$DyCl_3$ (0.50 mol%) system at 873 K. The microstructure was studied by electron microscopy and energy-dispersive X-ray spectrometry analyses, and the mechanical strength of the formed Dy-alloys was evaluated using punch tests. The alloying rate was influenced by the electrolysis potential and significantly by the temperature. Phase separation into $DyNi_2$ and Cr–Mo was observed, and a layered structure perpendicular to the depth direction was formed. The pitch of the layered structure was found to depend on the electrolysis potential, suggesting that the diffusion rate of Cr and Mo determined the structure. The Dy-alloyed samples electrolyzed at a more negative potential in the LiCl–KCl–$DyCl_3$ melt exhibited a higher mechanical strength. The Dy-alloyed samples obtained in the LiF–CaF_2–DyF_3 melt at 1223 K and 1323 K exhibited a low mechanical strength owing to the large grain size of the agglomerated Cr–Mo alloy phase.

Keywords: rare earth, molten salt, recycling, electrochemical formation, Dy alloy, Hastelloy C-276

1. Introduction

The development of new energy vehicles (NEVs), such as hybrid electric vehicles (HEVs), plug-in hybrid vehicles (PHVs), battery electric vehicles (BEVs), and fuel cell vehicles (FCVs) has attracted considerable recent attention. The use of numerous permanent magnets in the motors of NEVs has led to an increase in demand for Nd–Fe–B magnets with high magnetic performance. The addition of Dy to Nd–Fe–B magnets is necessary to preserve their strong magnetic properties at high

operating temperatures (above 473 K) for use in NEVs. Dy is also added in Nd–Fe–B magnets used in wind power generators and air conditioners. Recycling of magnet scrap is essential for facilitating the permanent and widespread use of NEVs because the rare earth (RE) elements used in Nd–Fe–B magnets are produced only in a few countries due to uneven resource distribution. Therefore, a new and efficient recycling method must be developed to recover RE metals from magnet scrap. Several pyrometallurgical processes have been proposed and investigated for recycling RE metals, such as extraction into molten metal [1],[2], molten salt [3],[4], and molten slag [5], electrolysis in molten salt or ionic liquid [6],[7], and selective vaporization [8].

A process for the separation and recovery of RE metals from magnet scrap using molten salt and an alloy diaphragm has been developed by our group [7],[9]–[18]. The principle of the process is based on our finding that certain RE metals are rapidly alloyed and de-alloyed with iron-group (IG) metals via electrochemical methods in molten salts [19]. In this process, two molten salt electrolytes are separated by a RE–IG alloy diaphragm. Scrap of RE magnets is used as an anode and RE ions are dissolved into the molten salt in an anode chamber. Systematic separation of Nd/Pr and Dy is realized through the alloy diaphragm by exploiting the differences in the formation potential of RE–IG alloys and the diffusion rate of RE metals in the RE–IG alloys with respect to Nd/Pr and Dy. Certain RE element selectively penetrates alloy diaphragm to be recovered as a cathode deposit in the cathode chamber, and the other RE element remains in the anode chamber. The possibility of highly effective separation of RE metals has been demonstrated by the selective and electrochemical formation of RE–Ni alloys (RE = Nd, Pr, and Dy) in molten LiF–CaF_2–REF_3 and NaCl–KCl–$RECl_3$ salts at 1123 K [10]–[12],[16] and 973 K [13]–[16], respectively. Moreover, Konishi *et al.* reported the selective formation of RE–Ni alloys using the same technique in a LiCl–KCl melt at 723 K, and achieved a high separation mass ratio of Dy:Nd = 72:1 in the alloy sample [20]–[23]. Selective permeation of Dy through an alloy diaphragm consisting of $RENi_2$ in LiCl–KCl eutectic melts containing $RECl_3$ (RE = Nd, Dy, and La; 0.50 mol.%) at 723 K was recently demonstrated by our group [24]. However,

75 the brittleness and inferior durability of the RE–Ni alloys hindered their long-term use. Therefore,
76 several Ni-based alloys containing elements inert to Nd and Dy, such as Cr and Mo, were employed
77 to develop a more durable alloy diaphragm in our subsequent study; the mechanical strength of the
78 Dy-alloyed samples prepared in a molten LiF–CaF_2–DyF_3 salt at 1123 K was also measured [18].
79 Consequently, the mechanical strength of the Hastelloy C-276 alloy was confirmed to be improved
80 via precipitation strengthening.

81 The Dy-alloying behavior of Ni-based alloys in molten LiF–CaF_2 were investigated only at
82 1123 K in our previous study [18]. Therefore, since higher reaction rate is expected at increased
83 temperatures, the effects of temperature from 1123 to 1323 K on alloying behavior and mechanical
84 strength were investigated in the present study. In addition, the results were compared with those
85 obtained in molten LiCl–KCl–$DyCl_3$ at 873 K to further discuss the effects of temperature. The effects
86 of the electrolysis potential on alloying behavior and mechanical strength were also explored. The
87 fabricated Dy alloys were examined by X-ray diffraction (XRD), cross-sectional scanning electron
88 microscopy (SEM), scanning transmission electron microscopy (STEM), and energy-dispersive X-
89 ray spectrometry (EDX). The mechanical strength of the formed Dy-alloys was evaluated using punch
90 tests.
91

92 **2. Experimental**

93 Details of the experimental setup and procedures employed for preparing the molten fluoride
94 system have been reported in our previous studies [13],[18]. LiF (Fuji Film Wako Pure Chemical
95 Corp., >98%) and CaF_2 (Kojundo Chemical Laboratory Co., Ltd., 99.9%) were mixed to the eutectic
96 composition (LiF:CaF_2 = 80.5:19.5 mol%). The eutectic mixture (300 g) was loaded into a graphite
97 crucible (Toyo Tanso Co., Ltd., IG-110, i.d. 90 mm × height 120 or 150 mm) and dried under vacuum
98 at 453 K for 72 h. The crucible was subsequently placed at the bottom of a stainless-steel vessel in an
99 airtight Kanthal container and further dried under vacuum at 773 K for 24 h. Electrochemical

measurements were conducted under an Ar atmosphere. DyF_3 powder (Kojundo Chemical Laboratory Co., Ltd., 99.9%) was added directly to the melts. For the experiments in the molten chloride system, LiCl (Fuji Film Wako Pure Chemical Corp., >99%) and KCl (Fuji Film Wako Pure Chemical Corp., 99%) were mixed to the eutectic composition (LiCl:KCl = 58.5:41.5 mol.%). The eutectic mixture (200 g) was loaded into an alumina crucible (Nikkato Corp., SSA-S, i.d. 64 mm × height 160 mm), which was subsequently placed at the bottom of an airtight Kanthal container. Some of these experiments were conducted in an Ar glove box. The residual moisture was removed by Ar bubbling at 873 K for several hours. $DyCl_3$ powder (Kojundo Chemical Laboratory Co., Ltd., 99.9%) was added to the melts.

Three types of electrodes were used as the working electrodes: wire (1.0 mm in diameter), plate (10-mm-wide × 10-mm-long × 0.1-mm-thick), and flag (diameter: 3.0 mm, thickness: 0.1 mm, lead wire diameter: 0.1 mm) [25]. Hastelloy C-276® (Nilaco Corp.), Ni (Nilaco Corp., >99%), and Mo (Nilaco Corp., 99.95%) were used as materials for the working electrodes. Hastelloy C-276® contains Ni as the primary constituent element (Ni, Cr, Mo, Fe, and W: <57, 14.5–16.5, 15–17, 4–7, and 3–4.5 wt%, respectively). A Pt wire (Tanaka Kikinzoku Kogyo Corp., 99.95%, diameter: 1 or 2 mm) immersed in the bulk melt was used as a quasi-reference electrode in the fluoride melt. A Ag wire (Nilaco Corp., 99.99%, diameter: 1 mm) immersed in LiCl–KCl–AgCl (1.0 mol%) contained in a Pyrex tube with a thin bottom (diameter: 6 mm) was used as a reference electrode in the chloride melt. The potentials of the reference electrodes were calibrated with reference to the potential of the Li^+/Li dynamic reference electrode, which was prepared by electrodepositing Li metal on a Mo electrode. The potentials obtained in voltammetry and open-circuit potentiometry are given with reference to this Li^+/Li potential. On the other hand, the electrolysis potentials are shown with reference to the equilibrium potential of $DyNi_3$/$DyNi_2$ in the respective molten salts [described henceforth as E_{eq} ($DyNi_3$/$DyNi_2$)]. A glassy carbon rod (Tokai Carbon Co., Ltd., diameter: 3.0 mm or 5.0 mm, immersion depth: 10 mm) was used as the counter electrode. During certain experiments in

the fluoride melt, a graphite rod (Nippon Techno-Carbon Co., Ltd., IGS-743K II, diameter: 9.0 mm) was inserted into the melt and contacted with the bottom of the graphite crucible. In this case, both the graphite rod and the interior part of the graphite crucible served as the counter electrode. An electrochemical measurement system (Hokuto Denko Corp., HZ-7000 or HZ-Pro) connected to a personal computer was used for the measurement. Alloy samples were prepared by potentiostatic electrolysis of the plate-type electrodes. The samples electrolyzed in the fluoride melt were analyzed without washing. By contrast, the samples electrolyzed in the chloride melt were washed with ion exchange water. Cross-sections of the alloy samples were analyzed by SEM (Thermo Fisher Scientific Inc., Phenom Pro Generation 5, or Hitachi Hitech Co., Ltd., TM–4000 plus) and STEM (Philips, Tecnai Osiris). Samples were embedded in resin and polished with emery paper and polycrystalline diamond or alumina suspension for SEM analysis. Certain samples were coated with Au to impart conductivity. The compositions of the samples were analyzed by EDX (Thermo Fisher Scientific Inc., SE1200–8001, or Oxford Instruments, AZtecOne). After SEM analysis, the fluoride salts covering the alloy samples were removed using a hand grinder (Kiso Power Tool Mfg. Co., Ltd, No. 28525-S). Subsequently, the alloy phases were identified by XRD (Rigaku Corp., Ultima IV, or Bruker Co., Ltd., D2 PHASER). To evaluate a durability of alloy diaphragm, the mechanical strength of the alloy samples was evaluated using shear punch tests. Each alloy sample (10-mm-wide × 10-mm-long × 0.17-mm-thick) was sandwiched between two acrylic plates and subjected to the shear punch test at around 293 K room temperature using a 2-mm-diameter stainless-steel punch attached to a load cell (IMADA, ZTS-500N). The feed rate of the punch was manually controlled to approximately 0.1 mm s^{-1}, and the maximum load prior to sample cracking was measured. The maximum load was measured at several different locations to obtain an average value, which was used to evaluate shear stress as a parameter to estimate the mechanical strength.

3. Results and Discussions

3.1. Formation rate of Dy alloys

3.1.1 Fluoride system

Figure 1 compares cyclic voltammograms obtained using the Hastelloy C-276 (HC) flag electrode in the molten LiF–CaF_2–DyF_3 (0.30 mol%) system at 1123 [17], 1223, and 1323 K. Voltammograms for the Ni flag electrode are also shown for reference. The cathodic currents (A) of the Ni electrode at 1123 K (Fig. 1(a)) observed from 0.7 V (vs. Li^+/Li) in the scan along the negative direction correspond to the formation of Dy–Ni alloys, as reported previously [17]. The formation of Dy–Ni alloys with high concentrations of Dy are indicated by the cathodic currents (B) and (C). The voltammogram for the HC electrode at 1123 K shows smaller cathodic currents and larger overpotentials than those for the Ni electrode owing to the agglomerated Cr–Mo phase impeding the diffusion of Dy in the alloy layer. Four anodic peaks corresponding to the dissolution of Dy from the different Dy–Ni alloy phases are observed after the reversal of the scanning direction. With the increase in temperature, larger cathodic currents for the voltammograms at 1223 K and 1323 K (Figs. 1(b) and (c)) than that at 1123 K (Fig. 1(a)) are observed. The larger cathodic currents for peaks (A) and (B) result in the disappearance of peak (C) at 1323 K. Additionally, the overpotential required for the formation of the Dy–Ni alloy becomes small or negligible. The peak shapes of the anodic current are ambiguous at higher temperature owing to the fast diffusion of Dy in the formed Dy–Ni alloys. Whereas these differences are observed, there are no other dramatic change in the voltammograms. These behaviors are not surprising because the alloys are almost identical intermetallic compounds at these temperatures, except for Dy_3Ni_2, according to the phase diagram of the Dy–Ni system [26].

*** Figure 1 ***

Similar electrolysis conditions were used for the preparation of Dy-alloyed samples from HC plate electrodes at −0.03, −0.08, −0.13, and −0.18 V vs. E_{eq} ($DyNi_3$/$DyNi_2$) for 10 min in molten

175 $LiF–CaF_2–DyF_3$ (0.50 mol%) at each temperature. The values of E_{eq} ($DyNi_3/DyNi_2$) determined by
176 open-circuit potentiometry for the HC wire electrode were 0.38 V (1123 K), 0.37 V (1223 K), and
177 0.36 V (1323 K) vs. Li^+/Li. All the cathodic current densities measured during the preparation of the
178 alloy samples were above 100 mA cm^{-2}. Figure 2 shows the XRD patterns of the samples prepared
179 at −0.08 V vs. E_{eq} ($DyNi_3/DyNi_2$) at 1123, 1223, and 1323 K. The formation of $DyNi_2$ and $DyNi_3$ was
180 confirmed at these temperatures. The intensities of the peaks attributed to $DyNi_3$ increase with the
181 increase in temperature. In contrast to the reported rapid and preferential formation of $RENi_2$ in
182 molten salts at 723–1123 K [10]–[23], especially in LiCl–KCl melts, the preferential formation of
183 only the $DyNi_2$ phase is found to be less significant in the $LiF–CaF_2$ melt at high temperatures.
184
185 *** Figure 2 ***
186
187 The rate of formation of the Dy alloys was evaluated by cross-sectional SEM analysis of all
188 the prepared samples, as shown in Fig. 3. The potentials mentioned in yellow on the images indicate
189 the values with respect to Li^+/Li. The alloy layers are 20–40-μm-thick at all investigated temperatures
190 at −0.03 V vs. E_{eq} ($DyNi_3/DyNi_2$), and increase in thickness at more negative potentials. The increase
191 is more prominent at higher temperatures, and the entire electrode appears to be alloyed at −0.18 V
192 at 1223 K and −0.13 V and −0.18 V at 1323 K. The theoretical thickness of the alloyed sample when
193 $DyNi_2$ is formed over the entire electrode is approximately 170 μm, which is in good agreement with
194 the thickness of the samples at −0.18 V at 1223 K and −0.13 V at 1323 K. On the other hand, a thicker
195 sample (~300 μm) is obtained at −0.18 V and 1323 K. This can be explained by the formation of the
196 DyNi phase in addition to $DyNi_2$; EDX analysis indicates that the atomic ratios of the dark and bright
197 grey areas in the cross-section are Dy:Ni = 1:1.9 and 1:1.1, respectively. This sample was considered
198 to be in a transition state during the preferential and rapid formation of $DyNi_2$, followed by DyNi,
199 which is the stable phase at this potential. The thicknesses of the Dy–HC alloy layer at each potential

and temperature are plotted in Fig. 4. The thickness of the alloy layer clearly tends to increase as the potential becomes more negative; the increasing trend becomes more pronounced as the temperature increases.

*** Figure 3 ***

*** Figure 4 ***

3.1.2 Chloride system

Cyclic voltammetry and potentiostatic electrolysis were also conducted in molten LiCl–KCl–$DyCl_3$ (0.50 mol%) at 873 K. Figure 5(a) shows cyclic voltammograms for the HC and Ni electrodes. In the scan along the negative direction, the cathodic currents (A) representing the formation of Dy–Ni alloys start at approximately 1.0 V vs. Li^+/Li for both the HC and Ni electrodes. In the case of the Ni electrode, the cathodic currents (B) sharply increase at 0.6 V owing to the formation of Dy–Ni alloys with high concentrations of Dy. The equilibrium potentials of Dy^{3+}/Dy and $DyNi_3$/$DyNi_2$ are known to be 0.48 V [27] and 0.77 V [28] vs. Li^+/Li at 873 K, respectively. In the case of the HC electrode, the increase in current (B) proceeds more slowly; However, the peak current density (approximately −0.1 A cm^{-2}) is almost similar for both the Ni and HC electrodes. This value is smaller than that of the molten fluoride system at 1123 K (Fig. 1(a)), indicating that the rate of alloy formation is lower in the LiCl–KCl–$DyCl_3$ system at 873 K than that in the LiF–CaF_2–DyF_3 system at 1123–1323 K. Therefore, the effect of temperature on the rate of alloy formation rate is significant.

The Dy-alloyed sample was prepared by potentiostatic electrolysis of the HC plate electrode at 0.60 V vs. Li^+/Li for 262 min; this potential was selected because it corresponded to the rapid increase in current (B) shown in Fig. 5(a). The potential is equivalent to −0.17 V vs. E_{eq} ($DyNi_3$/$DyNi_2$) = 0.77 V [28], which can be regarded as almost the same overpotential as −0.18 V vs.

225 E_{eq} ($DyNi_3$/$DyNi_2$) in the fluoride system shown in Fig. 3. The cathodic current during the electrolysis
226 was as low as approximately 10 mA cm^{-2}. The XRD pattern of the sample (Fig. 5(b)) indicates that
227 the obtained alloy is primarily composed of the $DyNi_2$ phase. Alloy samples for cross-sectional SEM
228 analysis were prepared by electrolysis at −0.17 V for 87 min and at −0.27 V for 33 min. As shown in
229 Figs. 5(c) and (d), the formed Dy–HC alloy layers are 40- (−0.17 V for 87 min) and 50-μm-thick
230 (−0.27 V for 33 min), respectively. Compared to the thicknesses of the Dy–HC alloy layers formed
231 in 10 min in the LiF–CaF_2–DyF_3 melt at 1123–1323 K (Fig. 3), the growth rate is ten to thirty times
232 smaller in the LiCl–KCl–$DyCl_3$ melt at 873 K, even at nearly the same overpotential required for
233 $DyNi_2$ formation. Additionally, the growth rate was observed to be nearly zero when the HC plate
234 electrode was electrolyzed in the LiCl–KCl–$DyCl_3$ melt at 723 K at a similar potential. This result
235 also shows that temperature has a significant effect on the rate of formation of the alloy layer.
236 Although the effect of constituent anions of molten salts on the formation rate of the alloy
237 layer was not investigated by using HC electrodes in this study, it can be discussed based on the
238 previously reported formation of $DyNi_2$ from pure Ni substrates, since the main component of HC is
239 Ni. In molten LiF–CaF_2–DyF_3 (0.30mol%) at 1123 K, a 90-μm thick $DyNi_2$ layer was obtained by
240 potentiostatic electrolysis at −0.20 V vs. E_{eq} ($DyNi_3$/$DyNi_2$) for 120 min [12]. Meanwhile, in molten
241 NaCl–KCl–$DyCl_3$ (0.50 mol%) at 973 K, a $DyNi_2$ layer with a thickness of more than 200 μm was
242 obtained at −0.23 V vs. E_{eq} ($DyNi_3$/$DyNi_2$) for 40 min [14]. Since the electrolysis potentials are almost
243 the same, these results clarify that the formation rate of $DyNi_2$ is higher in molten chlorides even at a
244 lower temperature. Regarding the kinetics of $DyNi_2$ formation, there is a report on the electrolysis of
245 pure Ni substrates in molten LiCl–KCl at 700 K [29]. The growth of the alloy film was observed to
246 increase linearly in thickness with respect to the electrolysis time at least up to 300 minutes, indicating
247 that the growth cannot be explained by the lattice diffusion mechanism. The large Dy diffusivity was
248 explained by the possibility of formation of microscopic cracks and/or grain boundaries that serve as
249 fast diffusion paths, which was supported by cross-sectional TEM for Pr–Ni alloys prepared in LiCl–

250 KCl–$PrCl_3$ (0.50 mol%) at 723 K [30]. The larger rate of $DyNi_2$ formation in the molten chlorides
251 may be due to the microscopic cracks and/or grain boundaries.
252
253 *** Figure 5 ***
254
255 3.2. Structure and mechanical strength of Dy alloys
256 The structural changes associated with phase separation in the Dy-alloying reaction were
257 analyzed by cross-sectional SEM/EDX of the samples shown in Fig. 3. Fig. 6 shows representative
258 cross-sectional SEM images and EDX mapping images of the samples obtained at (a) 1123 K, −0.18
259 V vs. E_{eq} ($DyNi_3$/$DyNi_2$), (b) 1123 K, −0.03 V, (c) 1323 K, −0.18 V, and (d) 1323 K, −0.03 V. The
260 object elements of EDX analysis are Dy, Ni, Cr, and Mo. Dark spots are visible in the bright matrix
261 for all the samples in the SEM images. This observation is similar to the results previously obtained
262 by our group at 1123 K and −0.18 V vs. E_{eq} ($DyNi_3$/$DyNi_2$) [17],[18]. The dark spots correspond to
263 the agglomerated Cr-rich Cr–Mo or Mo-rich Mo–Cr phases, whereas the bright matrix corresponds
264 to the formed Dy–Ni alloy. The typical compositions of the Dy alloy and the agglomerated phases are
265 summarized in Table 1. Phase separation occurs owing to the absence of the Cr–Dy and Mo–Dy alloy
266 phases [31].
267 A comparison of the structures of the samples prepared at −0.18 V at 1123 K (Fig. 6(a)) and
268 1323 K (Fig. 6(c)) reveals the effects of temperature on the structure of the formed alloy in terms of
269 the size and composition of the agglomerated phases. The Cr–Mo and Mo–Cr phases were found to
270 be 0.2–1 μm and 50–100 nm in size, respectively, at 1123 K through TEM/EDX mapping in our
271 previous study [18]; the SEM image in Fig. 6(a) shows a similar result. The dark spots in the SEM
272 image in Fig. 6(c) are clearly larger at a high temperature of 1323 K. Considering the composition of
273 the agglomerated phases, the formed Dy–Ni alloy has a composition corresponding to $DyNi_2$ at all
274 investigated temperatures; however, the agglomerated phases exhibit differences, with Cr-rich Cr–

Mo and Mo-rich Mo–Cr phases being present at 1123 K and a single Cr–Mo phase at 1323 K. The phase separation behavior at 1123 K was explained in our previous study [18] by the fact that the solid miscibility gap exhibited by the Cr–Mo system at ~39 at.% of Mo at the critical temperature of 1153 K [32]. According to the reported phase equilibria in the Ni–Cr–Mo system at 1123 K (Fig. 7(a)) [33], the value of the nominal composition of the phase precipitated from the Dy-alloyed HC plate varies along the blue arrow toward the final composition (A), Mo:Cr = 52:48 at% (excluding other elements). Consequently, the phases are separated into (B) Cr-rich Cr–Mo and (C) Mo-rich Mo–Cr phases. On the other hand, the phase equilibrium at 1323 K (Fig. 7(b)) indicates that the precipitated phase does not undergo phase separation because of its temperature being higher than the critical temperature. Therefore, a single Cr–Mo phase is precipitated.

The effect of electrolysis potential on phase separation can also be analyzed using the results shown in Fig. 6. At 1123 K, the sample at −0.18 V (Fig. 6(a)) exhibits homogeneous phase separation at the indicated magnification, whereas the sample at −0.03 V (Fig. 6(b)) shows ~0.5-μm-thick repeated Ni/Dy-rich and Cr/Mo-rich layers in the direction perpendicular to the depth direction. The latter suggests the formation of a layered structure, which is denoted as a mille-feuille structure henceforth; the separation is more evident at 1323 K. In the sample at −0.18 V (Fig. 6(c)), 0.5–3-μm-sized dark spotted patterns corresponding to the Cr–Mo phase are uniformly distributed in the Dy–Ni alloy matrix. Here, the composition of the Cr–Mo phase was almost constant. Additionally, the mille-feuille structure is partially visible in the EDX mapping results. At a more positive potential of −0.03 V (Fig. 6(d)), the mille-feuille structure consisting of Ni/Dy-rich and Cr/Mo-rich layers is clearly observed; these appear as bright and dark grey layers in the SEM image, respectively. The EDX mapping images suggest that the thicknesses of the Cr/Mo-rich and Ni/Dy-rich layers are 2–5 μm and 5–12 μm, respectively. The interval of the mille-feuille structure is approximately 10–15 μm. These images indicate that the structure exhibits a clear mille-feuille arrangement at positive potentials where the alloying rate is slow. On the other hand, the agglomeration of the Cr–Mo phase progresses

more at negative potentials where the alloying reaction is faster.

*** Figure 6 ***

*** Table 1 ***

*** Figure 7 ***

The relationship between the rate of alloy formation and their structures is clearer for the samples electrolyzed in the chloride melt. Figure 8 shows the cross-sectional SEM images for the alloy samples obtained at (a) −0.17 V, (b) −0.22 V, and (c) −0.27 V vs. E_{eq} ($DyNi_3/DyNi_2$) in the LiCl–KCl–$DyCl_3$ melt at 873 K. The charge density was set to 50 C cm^{-2}. Mille-feuille structures consisting of dark and light grey areas are observed in all the samples. Figure 9 shows the cross-sectional EDX mapping images of the sample at −0.17 V (shown in Fig. 8(a)), which indicate that the bright and dark grey areas correspond to the $DyNi_2$ and enriched Cr–Mo phases, respectively. The interval of the mille-feuille structure observed in the SEM images is larger at more positive potentials, that is, 2–3 μm at −0.17 V and 1 μm at −0.27 V (Fig. 8). This relationship between the phase separation distance and the electrolysis potential is similar to that observed in the fluoride melt. These trends indicate that the alloy structure is determined by the balance between the alloying rate and the rate of atomic diffusion. During the rapid formation of the alloy, the duration for atomic diffusion is short and agglomeration occurs over a small range, resulting in short intervals and/or small agglomerates. Moreover, Ni and Dy are considered to diffuse faster to form Dy–Ni alloys owing to the large driving force of diffusion, whereas Cr and Mo are expected to diffuse comparatively slowly. In the case of the slow formation of alloys, diffusion occurs over long distances, and forms a mille-feuille structure at long intervals.

*** Figure 8 ***

325 *** Figure 9 ***

326

327 The difference in the structure of the precipitated phases in the alloy layer presumably affects
328 their mechanical strength; therefore, the strength at which cracking occurs in the Dy-alloyed samples
329 was measured and converted to shear stress. Figure 10 compares the converted shear stresses of the
330 Dy-alloyed HC plates prepared at several potentials in LiF–CaF_2–DyF_3 at 1123–1323 K and LiCl–
331 KCl–$DyCl_3$ at 873 K. In the chloride system (Fig. 10(b)), the shear stress is higher at more negative
332 potentials, for example, 32 ± 5 N mm^{-2} at −0.195 V and 140 ± 50 N mm^{-2} at −0.27 V. In the fluoride
333 system (Fig. 10(a)), the effect of the potential on shear stress is comparatively smaller at 1123 K, for
334 example, 14 N mm^{-2} at −0.13 V and 24 ± 6 N mm^{-2} at −0.18 V; almost no dependence is observed at
335 1223 K and 1323 K. However, the effect of electrolysis temperature is observed in the fluoride melt.
336 The shear stress of the sample at −0.18 V decreases from 24 ± 6 N mm^{-2} at 1123 K to 15 ± 1 N mm^{-2}
337 at 1323 K.

338 The effects of electrolysis temperature and potential on the mechanical strength of the
339 formed Dy-alloyed samples are possibly caused by the structure of the Cr–Mo phase. Two
340 representative samples were examined by STEM to confirm this. Figure 11 shows the STEM and
341 EDX mapping images of the center of the Dy-alloy layer of the samples prepared in the fluoride melt
342 at 1323 K and the chloride melt at 873 K. In the fluoride system (Fig. 11(a)), the 200–1000-nm-sized
343 Cr–Mo phase is separated from the Dy–Ni phase. The large size and distance of the Cr–Mo particles
344 are due to the high rate of diffusion of Cr and Mo. Shorter distances between the precipitated particles
345 are known to be key for facilitating precipitation strengthening; therefore, the long distance between
346 the Cr–Mo particles deteriorates the mechanical strength, especially at temperatures higher than the
347 critical temperature of the Cr–Mo system (1223 K and 1323 K). Typical precipitation strengthening,
348 including Ni-based alloys, requires a fine dispersion of the phases at less than 100 nm in distance
349 [34]–[36]. In the case of the sample at −0.18 V at 1123 K (Fig. 6(a) and Ref. [17][18]), the

agglomerated Cr–Mo phase is evenly distributed in the form of spots in the $DyNi_2$ phase. Although this distribution is larger than the 100-nm scale, the even distribution is likely responsible for its relatively higher mechanical strength compared to that of the other samples.

The dispersion state of the Cr–Mo phase is noticeably different in the chloride system. Although the Cr/Mo-rich layer seems to contain only Cr and Mo in the SEM image (Fig. 9), the images in Fig. 11(b) measured at the boundary of the Cr/Mo-rich and Ni/Dy-rich layers of the mille-feuille structure indicate that this layer contains both the Cr–Mo and Dy–Ni phases. Cr–Mo particles (10–20 nm in size) are dispersed in the Dy–Ni matrix. The distance between the Cr–Mo particles is also 10–20 nm, indicating their significant contribution to precipitation strengthening. Additionally, the higher shear stress at more negative potentials is attributed to the shorter interval of the mille-feuille structure. As previously mentioned, this tendency can be explained by the balance between the rate of alloy formation and the rates of diffusion of Cr and Mo. At a lower experimental temperature in the chloride system, Cr and Mo are almost immobile. More quantitative discussions can be facilitated if the original state of the substrate can be evaluated using, for example, the effect of rolling. In summary, the occurrence of the mille-feuille structure can be explained by the difference in the relative rates of diffusion of Dy/Ni and Cr/Mo.

The present study reveals that the control of the structure is important to achieve a diaphragm with a high mechanical strength for use in the RE separation process. In this regard, it is desirable to perform electrolysis at a temperature not exceeding the critical temperature of the Cr–Mo system and at a more negative potential, to aim for a narrow-pitch mille-feuille structure and/or a structure with fine aggregated phases.

*** Figure 10 ***

*** Figure 11 ***

4. Conclusion

This study investigated the Dy-alloying behavior of Hastelloy C-276 in molten LiF–CaF_2–DyF_3 at 1123–1323 K and molten LiCl–KCl–$DyCl_3$ at 873 K to develop a durable alloy diaphragm for use in the separation of rare earth metals from magnet scrap. The effects of temperature and electrolysis potential on the Dy-alloying rate, structure, and mechanical strength were examined. A mille-feuille structure perpendicular to the depth direction was observed in samples prepared in both the melts under conditions for the formation of $DyNi_2$. The interlayer distance of the mille-feuille structure was found to be affected by the electrolysis temperature and potential. Dy-alloyed samples with high mechanical strength were obtained when the interlayer distance was short. Electrolysis at a more negative potential was found to be preferable for obtaining a durable alloy diaphragm, especially in the chloride melt. In the fluoride melt, electrolysis at a temperature lower than the critical temperature of the Cr–Mo system was desirable.

Acknowledgments

A part of this study was conducted as commissioned research with the New Energy and Industrial Technology Development Organization (NEDO) of Japan.

REFERENCES

[1] Y. Xu, L.S. Chumbley, F.C. Laabs, Liquid Metal Extraction of Nd from NdFeB Magnet Scrap, J. Mater. Res. 15 (2000) 2296–2304. https://doi.org/10.1557/JMR.2000.0330

[2] O. Takeda, T.H. Okabe, Y. Umetsu, Phase Equilibrium of the System Ag–Fe–Nd, and Nd Extraction from Magnet Scraps using Molten Silver, J. Alloy. Compd. 379 (2004) 305–313. https://doi.org/10.1016/j.jallcom.2004.02.038

[3] S. Shirayama, T.H. Okabe, Current Status of Rare Earth Alloy Magnet and Pyrometallurgical Recycling Technology, Molten Salts 52 (2009) 71–82 (in Japanese).

[4] S. Shirayama, T.H. Okabe, Selective Extraction and Recovery of Nd and Dy from Nd-Fe-B Magnet Scrap by Utilizing Molten $MgCl_2$, Metall. Mater. Trans. B 49 (2018) 1067–1077. https://doi.org/10.1007/s11663-018-1176-0

[5] O. Takeda, K. Nakano, Y. Sato, Resource Recovery from Wastes of Rare Earth Magnet by Utilizing Fluoride Molten Salts, Molten Salts 52 (2009) 63–70 (in Japanese).

[6] M. Matsumiya, H. Kondo, A. Kurachi, K. Tsunashima, S. Kodama, Separation of Iron Group Metal and Recovery of Neodymium Metal by Electrodeposition in Ionic Liquids, J. Japan Inst. Metals **75** (2011) 607–612. https://doi.org/10.2320/jinstmet.75.607

[7] T. Oishi, H. Konishi, T. Nohira, Recovery Method of Rare Earth Metals through Electrolysis of Molten Salt, Japanese Patent (2014) JP 5504515.

[8] T. Uda, K.T. Jacob, M. Hirasawa, Technique for Enhanced Rare Earth Separation, Science 289 (2000) 2326–2329. https://doi.org/10.1126/science.289.5488.2326

[9] T. Oishi, H. Konishi, T. Nohira, M. Tanaka, T. Usui, Separation and Recovery of Rare Earth Metals by Molten Salt Electrolysis using Alloy Diaphragm, Kagaku Kogaku Ronbunshu, 36 (2010) 299–303 (in Japanese). https://doi.org/10.1252/kakoronbunshu.36.299

[10] T. Nohira, S. Kobayashi, K. Kobayashi, R. Hagiwara, T. Oishi, H. Konishi, Electrochemical Formation of Nd–Ni Alloys in Molten $LiF–CaF_2–NdF_3$, ECS Trans. 33 (2010) 205–212.

https://doi.org/10.1149/1.3484777

[11] S. Kobayashi, K. Kobayashi, T. Nohira, R. Hagiwara, T. Oishi, H. Konishi, Electrochemical Formation of Nd–Ni Alloys in Molten LiF–CaF_2–NdF_3, J. Electrochem. Soc., 158 (2011) E142–E146. https://doi.org/10.1149/2.072112jes

[12] S. Kobayashi, T. Nohira, K. Kobayashi, K. Yasuda, R. Hagiwara, T. Oishi, H. Konishi, Electrochemical Formation of Dy–Ni Alloys in Molten LiF–CaF_2–DyF_3, J. Electrochem. Soc. 159 (2012) E193–E197. https://doi.org/10.1149/2.053212jes

[13] K. Yasuda, S. Kobayashi, T. Nohira, R. Hagiwara, Electrochemical formation of Nd–Ni Alloys in Molten NaCl–KCl–$NdCl_3$, Electrochim. Acta 92 (2013) 349–355. https://doi.org/10.1016/j.electacta.2013.01.049

[14] K. Yasuda, S. Kobayashi, T. Nohira, R. Hagiwara, Electrochemical Formation of Dy–Ni Alloys in Molten NaCl–KCl–$DyCl_3$, Electrochim. Acta 106 (2013) 293–300. https://doi.org/10.1016/j.electacta.2013.05.095

[15] K. Yasuda, K. Kondo, T. Nohira, R. Hagiwara, Electrochemical Formation of Pr–Ni Alloys in LiF–CaF_2–PrF_3 and NaCl–KCl–$PrCl_3$ Melts, J. Electrochem. Soc. 161 (2014) D3097–D3014. https://doi.org/10.1149/2.012407jes

[16] K. Yasuda, K. Kondo, S. Kobayashi, T. Nohira, R. Hagiwara, Selective Formation of Rare-Earth–Nickel Alloys via Electrochemical Reactions in NaCl–KCl Molten Salt, J. Electrochem. Soc. 163 (2016) D140–D145. https://doi.org/10.1149/2.0501605jes

[17] Y. Watanabe, Y. Norikawa, K. Yasuda, T. Nohira, Electrochemical Dy-Alloying Behaviors of Inconel and Hastelloy in Molten LiF–CaF_2–DyF_3, Mater. Trans. 60 (2019) 379–385. https://doi.org/10.2320/matertrans.MA201805

[18] K. Yasuda, T. Enomoto, Y. Watanabe, T. Oishi, T. Nohira, Electrochemical Dy-Alloying Behaviors of Ni-Based Alloys in Molten LiF–CaF_2–DyF_3: Effects of Constituent Elements, Mater. Trans. 61 (2020) 2329–2335. https://doi.org/10.2320/matertrans.MT-M2020200

[19] H. Konishi, T. Nohira, Y. Ito, Formation and Phase Control of Dy Alloy Films by Electrochemical Implantation and Displantation, J. Electrochem. Soc. 148 (2001) C506–C511. https://doi.org/10.1149/1.1379031

[20] H. Konishi, H. Ono, T. Nohira, T. Oishi, Separation of Dy and Nd (La) Using Molten Salt and an Alloy Diaphragm, ECS Trans. 50 (2012) 463–472. https://doi.org/10.1149/05011.0463ecst

[21] T. Nohira, S. Kobayashi, K. Kondo, K. Yasuda, R. Hagiwara, T. Oishi, H. Konishi, Electrochemical Formation of RE–Ni (RE=Pr, Nd, Dy) Alloys in Molten Halides, ECS Trans. 50 (2012) 473–482. https://doi.org/10.1149/05011.0473ecst

[22] H. Konishi, H. Ono, E. Takeuchi, T. Nohira, T. Oishi, Separation of Dy from Nd–Fe–B Magnet Scraps Using Molten Salt Electrolysis, ECS Trans. 64 (2014) 593–600. https://doi.org/10.1149/06404.0593ecst

[23] H. Konishi, H. Ono, E. Takeuchi, T. Nohira, T. Oishi, Electrochemical Separation of Dy from Nd Magnet Scraps in Molten LiCl–KCl, Miner. Process. Extr. Metall. 125 (2016) 216–220. https://doi.org/10.1080/03719553.2016.1188482

[24] T. Oishi, M. Yaguchi, Y. Katasho, H. Konishi, T. Nohira, Selective Permeation of Dysprosium Through an Alloy Diaphragm in Molten Chloride Systems J. Electrochem. Soc. 167 (2020) 163505. https://doi.org/10.1149/1945-7111/abd0cc

[25] K. Maeda, K. Yasuda, T. Nohira, R. Hagiwara, T. Homma, Silicon Electrodeposition in Water-Soluble KF–KCl Molten Salt: Investigations on the Reduction of Si(IV) Ions, J. Electrochem. Soc. 162 (2015) D444–D448. https://doi.org/10.1149/2.0441509jes

[26] Y.Y. Pan, P. Nash, The Ni–Dy (Nickel–Dysprosium) System, in: P. Nash (Ed.), ASM International, Phase Diagrams of Binary Nickel Alloys, Materials Park, 1991, p. 96.

[27] H. Konishi, Doctor Thesis of Kyoto University (2003).

[28] H. Konishi, T. Nishikiori, T. Nohira, Y. Ito, Thermodynamic Properties of Dy–Ni Intermetallic Compounds, Electrochim. Acta 48 (2003) 1403–1408. https://doi.org/10.1016/S0013-

4686(03)00007-0

[29] H. Konishi, T. Nohira, Y. Ito, Kinetics of $DyNi_2$ Film Growth by Electrochemical Implantation, Electrochim. Acta 48 (2003) 563–568. https://doi.org/10.1016/S0013-4686(02)00723-5

[30] T. Nohira, H. Kambara, K. Amezawa, Y. Ito, Electrochemical Formation and Phase Control of Pr-Ni Alloys in a Molten LiCl-KCl-$PrCl_3$ System, J. Electrochem. Soc. 152 (2005) C183–C189. https://doi.org/10.1149/1.1864281

[31] T.B. Massalski, H. Okamoto, P.R. Subramanian, L. Kacprzak, Binary Alloy Phase Diagrams, 2nd edition, CD-ROM version 1.0, ASM International, Materials Park, 1990.

[32] M. Venkatraman, J.P. Neumann, Cr−Mo, Bull. Alloy Phase Diagrams 8 (1987) 289–290. https://doi.org/10.1007/BF02874921

[33] P.E.A. Turchi, L. Kaufman, Z.-K. Liu, Modeling of Ni–Cr–Mo Based Alloys: Part I—Phase Stability, Calphad. 30 (2006) 70–87. https://doi.org/10.1016/j.calphad.2005.10.003

[34] R.W. Kozar, A. Suzuki, W.W. Milligan, J.J. Schirra, M.F. Savage, T.M. Pollock, Strengthening Mechanisms in Polycrystalline Multimodal Nickel-Base Superalloys, Metall. Mater. Trans. A 40 (2009) 1588–1603. https://doi.org/10.1007/s11661-009-9858-5

[35] K.J. Ducki, Research of the Microstructure and Precipitation Strengthening in a High-Temperature Fe–Ni Superalloy, IOP Conf. Ser.: Mater. Sci. Eng. 35 (2012) 012007. https://doi.org/doi:10.1088/1757-899X/35/1/012007

[36] B. Gwalani, V. Soni, M. Lee, S. Mantri, Y. Ren, R. Banerjee, Optimizing the Coupled Effects of Hall-Petch and Precipitation Strengthening in a $Al_{0.3}$CoCrFeNi High Entropy Alloy, Mater. Des. 121 (2017) 254–260. https://doi.org/10.1016/j.matdes.2017.02.072

List of Captions

Table 1 Typical composition of the Dy alloy and separated phases determined by point EDX analysis of samples obtained by potentiostatic electrolysis of HC plate electrodes.

Figure 1 Cyclic voltammograms for Ni and HC flag electrodes in molten LiF–CaF_2–DyF_3 (0.30 mol%) at (a) 1123 K [17], (b) 1223 K, and (c) 1323 K at a scan rate of 50 mV s^{-1}.

Figure 2 XRD patterns of samples prepared by potentiostatic electrolysis of HC plate electrodes at −0.08 V vs. E_{eq} ($DyNi_3$/$DyNi_2$) for 10 min in molten LiF–CaF_2–DyF_3 (0.50 mol%) at (a) 1123 K, (b) 1223 K, and (c) 1323 K.

Figure 3 Cross-sectional SEM images of samples prepared by potentiostatic electrolysis of HC plate electrodes at each potential vs. E_{eq} ($DyNi_3$/$DyNi_2$) for 10 min in molten LiF–CaF_2–DyF_3 (0.50 mol%) at (a) 1123 K, (b) 1223 K, and (c) 1323 K. The values in yellow represent potentials vs. Li^+/Li.

Figure 4 Thickness of the Dy–HC alloy layer obtained by potentiostatic electrolysis at each potential for 10 min in molten LiF–CaF_2–DyF_3 (0.50 mol%) at 1123, 1223, and 1323 K.

Figure 5 (a) Cyclic voltammograms for Ni and HC electrodes at a scan rate of 50 mV s^{-1} in molten LiCl–KCl–$DyCl_3$ (0.50 mol%) at 873 K. (b) An XRD pattern of the sample prepared by potentiostatic electrolysis of an HC plate electrode at −0.17 V vs. E_{eq} ($DyNi_3$/$DyNi_2$) for 262 min. Cross-sectional SEM images of samples prepared by potentiostatic electrolysis of HC plate electrodes at (c) −0.17 V for 87 min and (d) −0.27

V for 33 min.

Figure 6 Cross-sectional SEM and EDX mapping images of samples obtained by potentiostatic electrolysis of HC plate electrodes in molten $LiF–CaF_2–DyF_3$ (0.50 mol%) for 10 min. Electrolysis conditions: (a) −0.18 V vs. E_{eq} ($DyNi_3/DyNi_2$) at 1123 K, (b) −0.03 V at 1123 K, (c) −0.18 V at 1323 K, and (d) −0.03 V at 1323 K.

Figure 7 Phase changes estimated using the evaluated isothermal sections of the Ni–Cr–Mo ternary phase diagram at (a) 1123 K and (b) 1323 K [33].

Figure 8 Cross-sectional SEM images of samples obtained by potentiostatic electrolysis of HC plate electrodes at (a) −0.17 V, (b) −0.22 V, and (c) −0.27 V vs. E_{eq} ($DyNi_3/DyNi_2$) in molten $LiCl–KCl–DyCl_3$ (0.50 mol%) at 873 K. A charge density of 50 C cm^{-2} is used.

Figure 9 Cross-sectional SEM and EDX mapping images of samples obtained by potentiostatic electrolysis of the HC plate electrode at −0.17 V vs. E_{eq} ($DyNi_3/DyNi_2$) for 260 min in molten $LiCl–KCl–DyCl_3$ (0.50 mol%) at 873 K. A charge density of 25 C cm^{-2} is used.

Figure 10 Shear stress of samples prepared by potentiostatic electrolysis of HC plate electrodes in (a) molten $LiF–CaF_2–DyF_3$ (0.30 or 0.50 mol%) at 1123–1323 K and (b) molten $LiCl–KCl–DyCl_3$ (0.50 mol%) at 873 K.

Figure 11 High-angle annular dark field STEM images and EDX mapping images of samples obtained by potentiostatic electrolysis of HC plate electrodes at (a) −0.08 V vs. E_{eq} ($DyNi_3/DyNi_2$) for 30 min at 1323 K in molten $LiF–CaF_2–DyF_3$ (0.50 mol%) and (b)

−0.17 V vs. E_{eq} ($DyNi_3/DyNi_2$) for 260 min in molten LiCl–KCl–$DyCl_3$ (0.50 mol%) at 873 K.

544 Table 1 Typical composition of the Dy alloy and separated phases determined by point EDX analysis

545 of samples obtained by potentiostatic electrolysis of HC plate electrodes.

546

Phase	Condition		Composition of element i, x_i / at%				
	Temperature / K	Potential / V vs. E_{eq} ($DyNi_3/DyNi_2$)	Dy	Ni	Cr	Fe	Mo
Dy alloy	1123 [a]	−0.18	30.9	66.1	0.5	1.9	0.6
	1323 [b]	−0.03	30.3	67.4	0.7	0.9	0.2
	873 [b]	−0.17	30.8	61.9	2.2	4.6	0.7
Agglomerated	1123 [a]	−0.18	7.9	0.9	76.7	2.9	11.2
			n.d.	10.7	44.2	14.0	29.2
	1323 [b]	−0.03	5.6	20.2	37.6	11.3	23.1
	873 [b]	−0.17	21.2	43.7	18.2	6.6	10.3

547 a: Measured by TEM/EDX in Ref. [18]

548 b: Measured by SEM/EDX

549 n.d.: not detected

(a) 1123 K

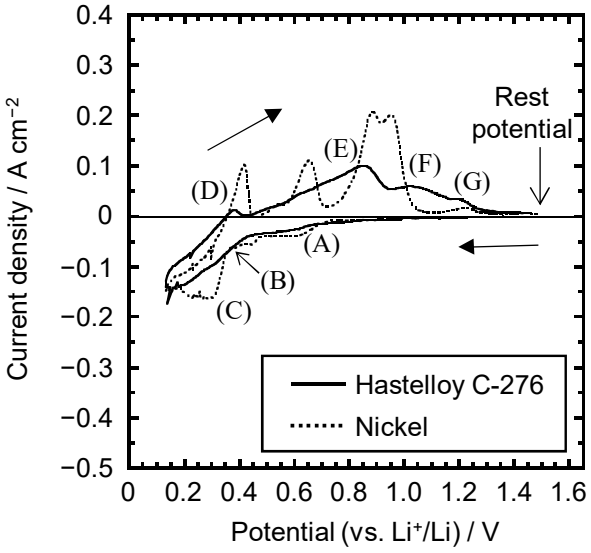

(b) 1223 K

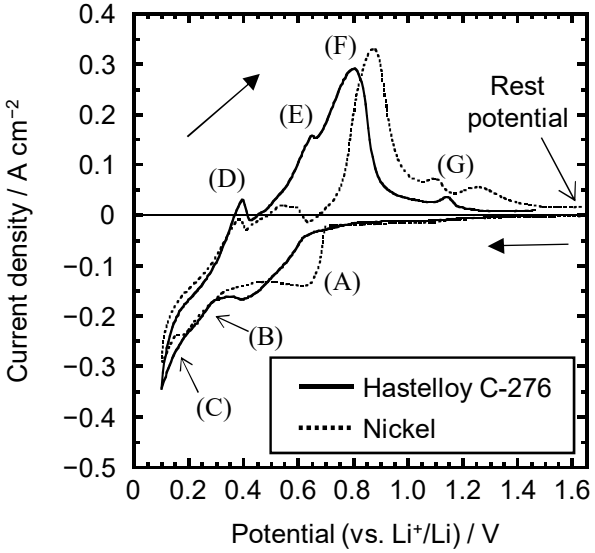

(c) 1323 K

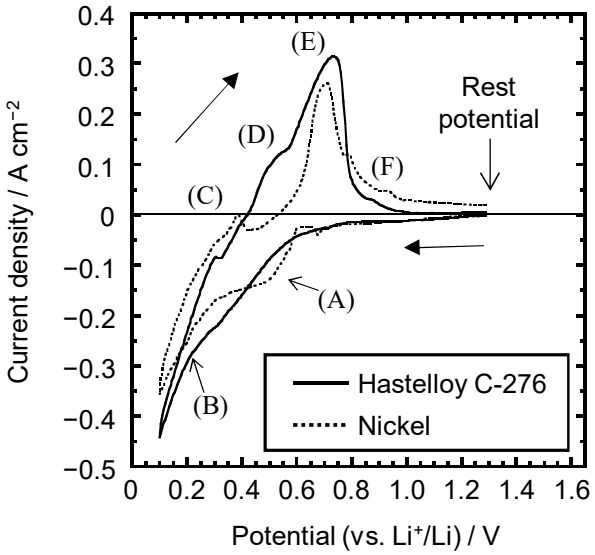

Fig. 1 Cyclic voltammograms for Ni and HC flag electrodes in molten LiF–CaF_2–DyF_3 (0.30 mol%) at (a) 1123 K [17], (b) 1223 K, and (c) 1323 K at a scan rate of 50 mV s^{-1}.

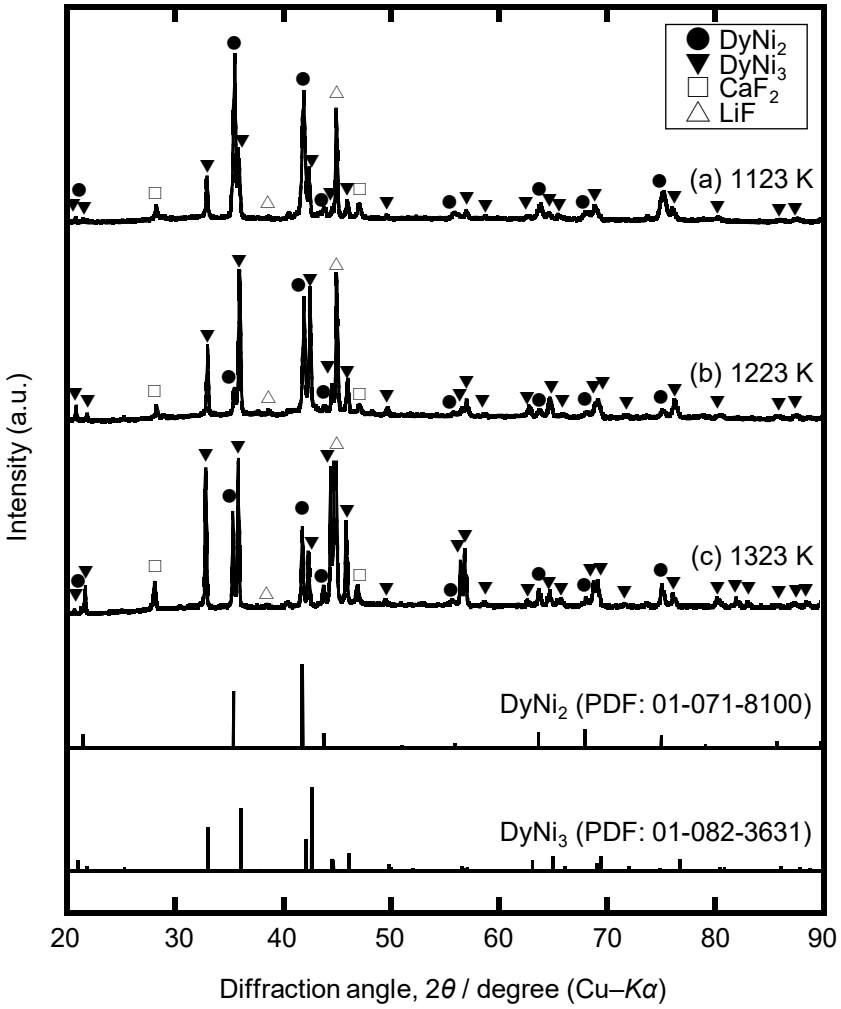

Fig. 2 XRD patterns of samples prepared by potentiostatic electrolysis of HC plate electrodes at −0.08 V vs. E_{eq} ($DyNi_3/DyNi_2$) for 10 min in molten $LiF–CaF_2–DyF_3$ (0.50 mol%) at (a) 1123 K, (b) 1223 K, and (c) 1323 K.

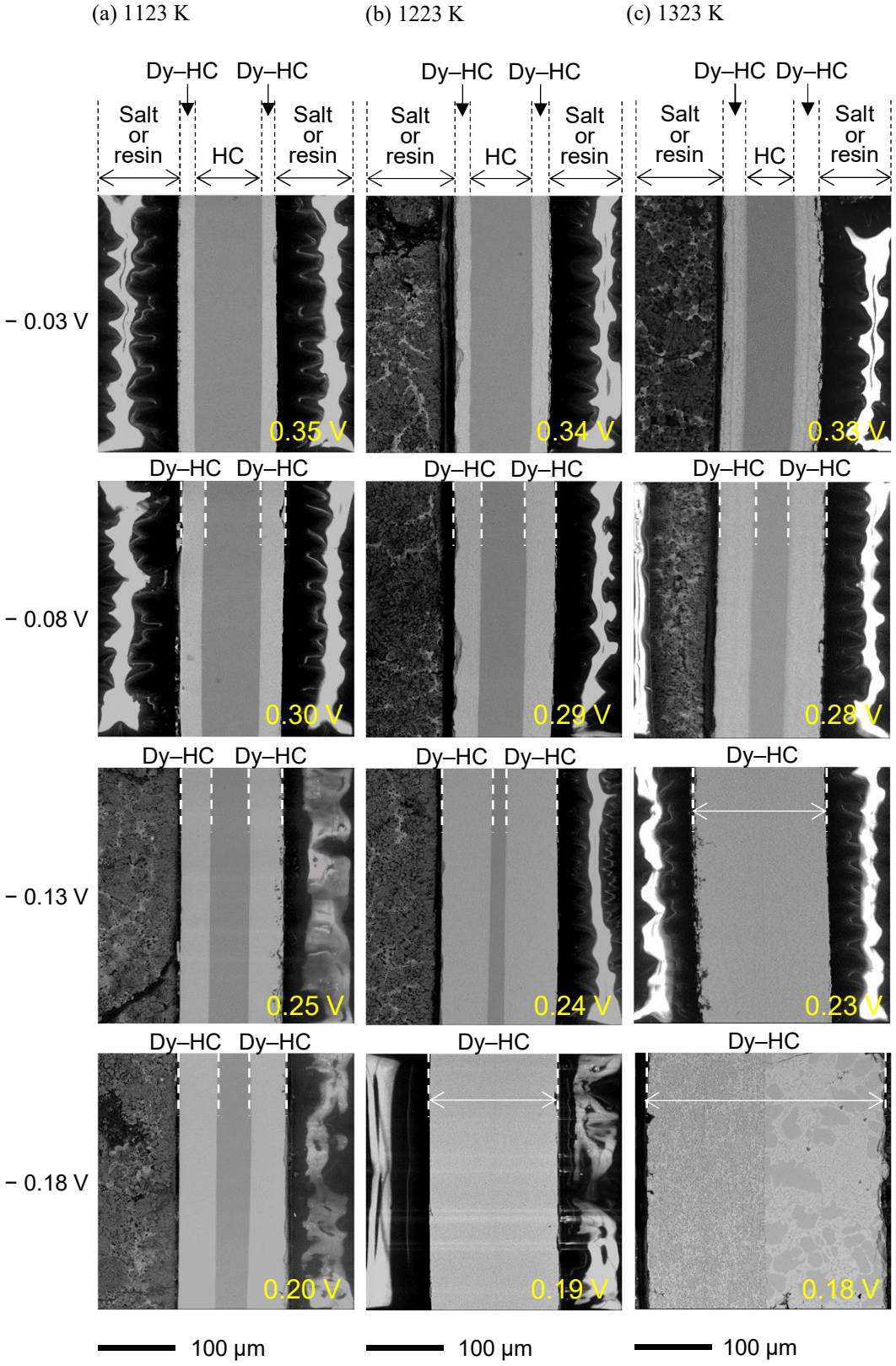

Fig. 3 Cross-sectional SEM images of samples prepared by potentiostatic electrolysis of HC plate electrodes at each potential vs. E_{eq} ($DyNi_3/DyNi_2$) for 10 min in molten $LiF–CaF_2–DyF_3$ (0.50 mol%) at (a) 1123 K, (b) 1223 K, and (c) 1323 K. The values in yellow represent potentials vs. Li^+/Li.

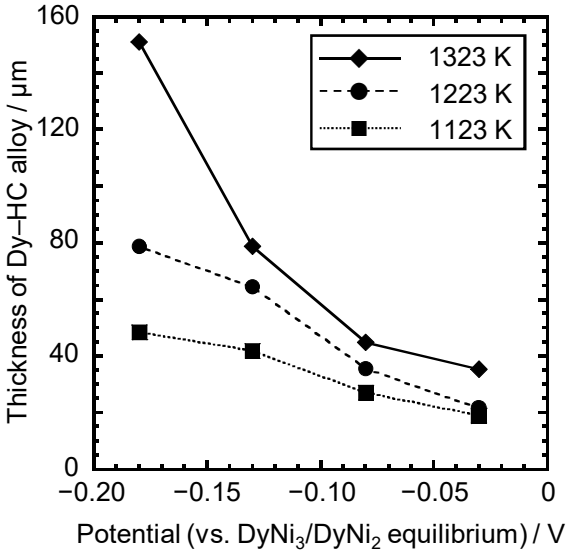

Fig. 4 Thickness of the Dy–HC alloy layer obtained by potentiostatic electrolysis at each potential for 10 min in molten LiF–CaF_2–DyF_3 (0.50 mol%) at 1123, 1223, and 1323 K.

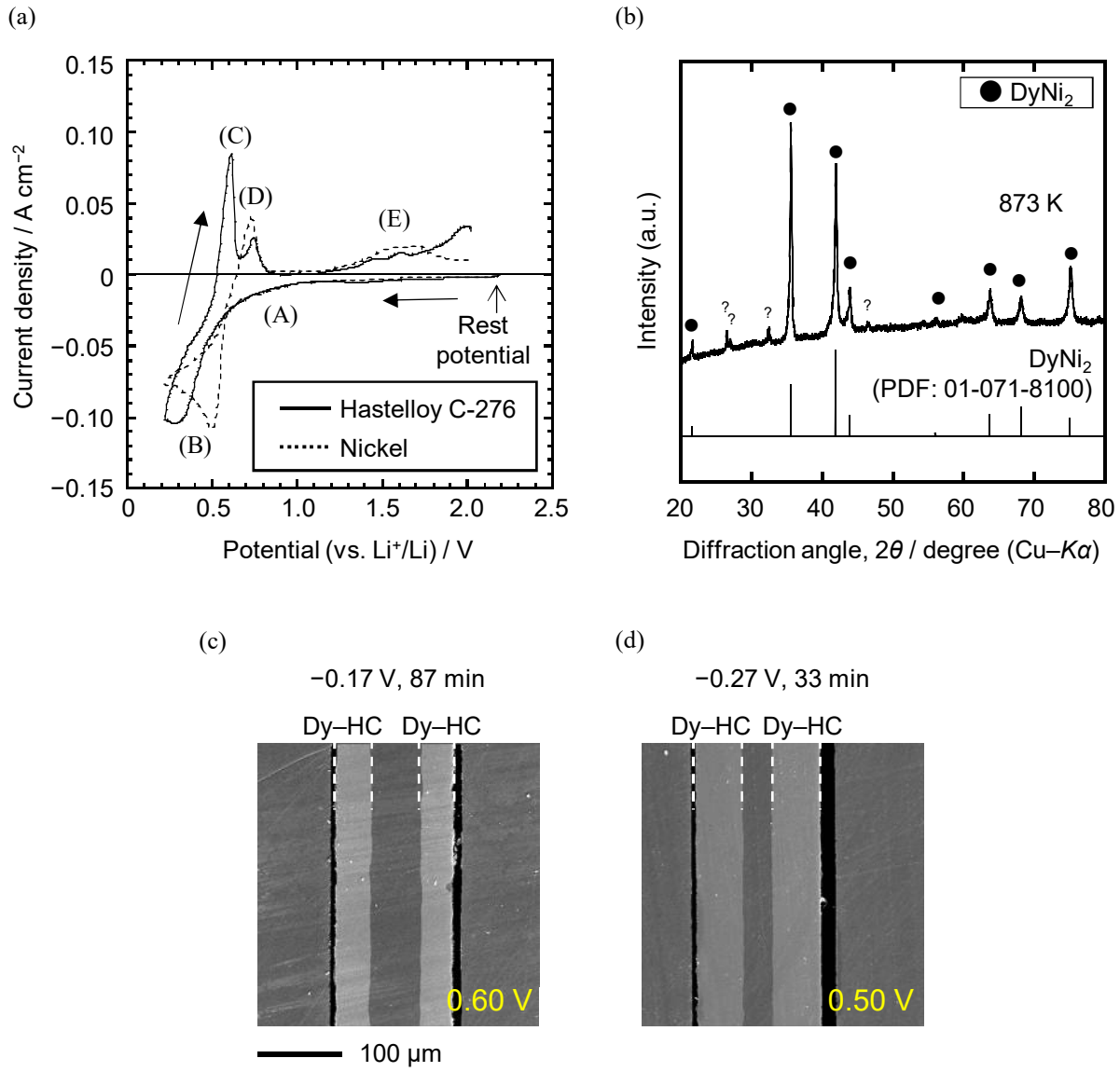

Fig. 5 (a) Cyclic voltammograms for Ni and HC electrodes at a scan rate of 50 mV s^{-1} in molten LiCl–KCl–$DyCl_3$ (0.50 mol%) at 873 K. (b) An XRD pattern of the sample prepared by potentiostatic electrolysis of an HC plate electrode at −0.17 V vs. E_{eq} ($DyNi_3$/$DyNi_2$) for 262 min. Cross-sectional SEM images of samples prepared by potentiostatic electrolysis of HC plate electrodes at (c) −0.17 V for 87 min and (d) −0.27 V for 33 min.

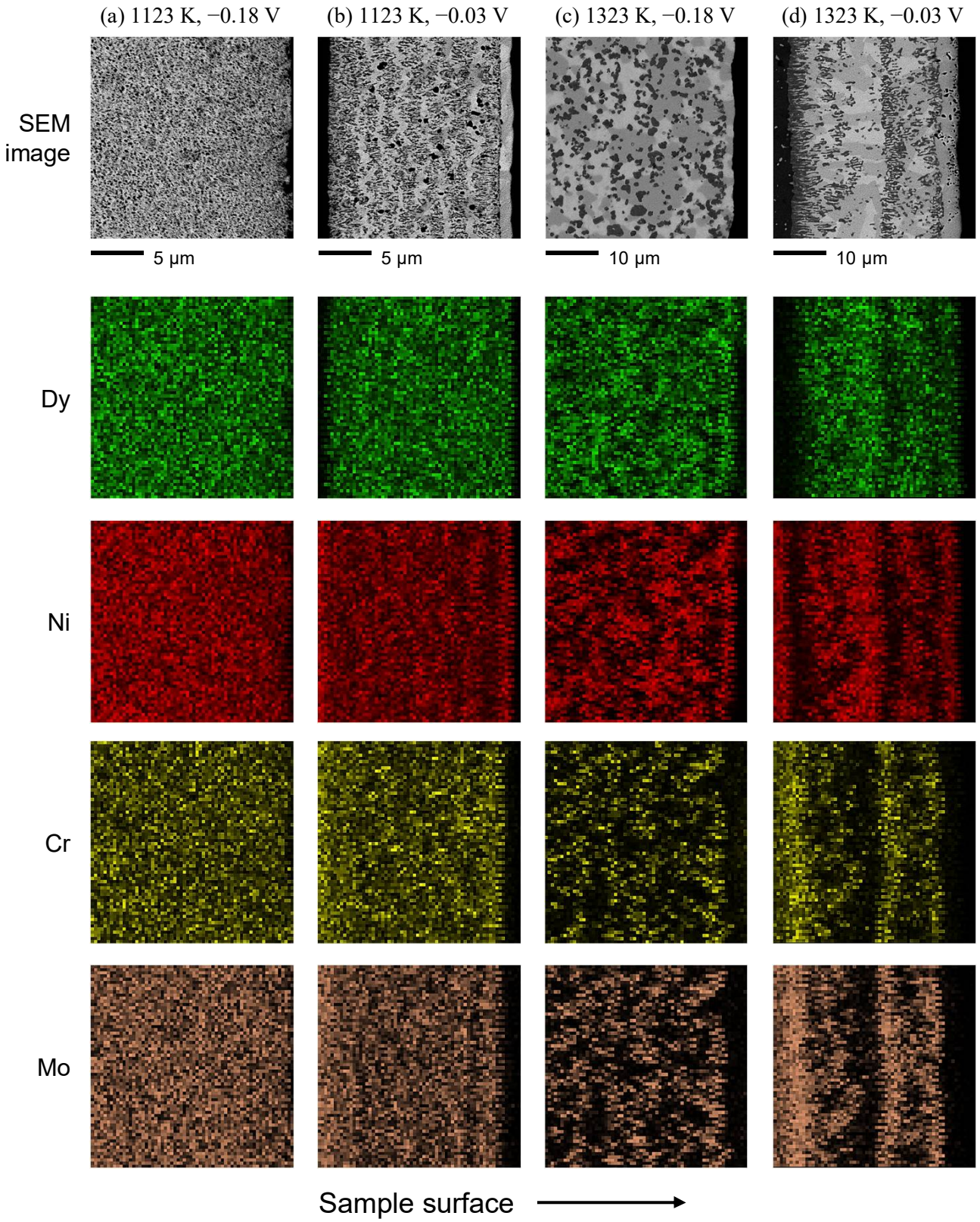

Fig. 6 Cross-sectional SEM and EDX mapping images of samples obtained by potentiostatic electrolysis of HC plate electrodes in molten LiF–CaF_2–DyF_3 (0.50 mol%) for 10 min. Electrolysis conditions: (a) −0.18 V vs. E_{eq} ($DyNi_3$/$DyNi_2$) at 1123 K, (b) −0.03 V at 1123 K, (c) −0.18 V at 1323 K, and (d) −0.03 V at 1323 K.

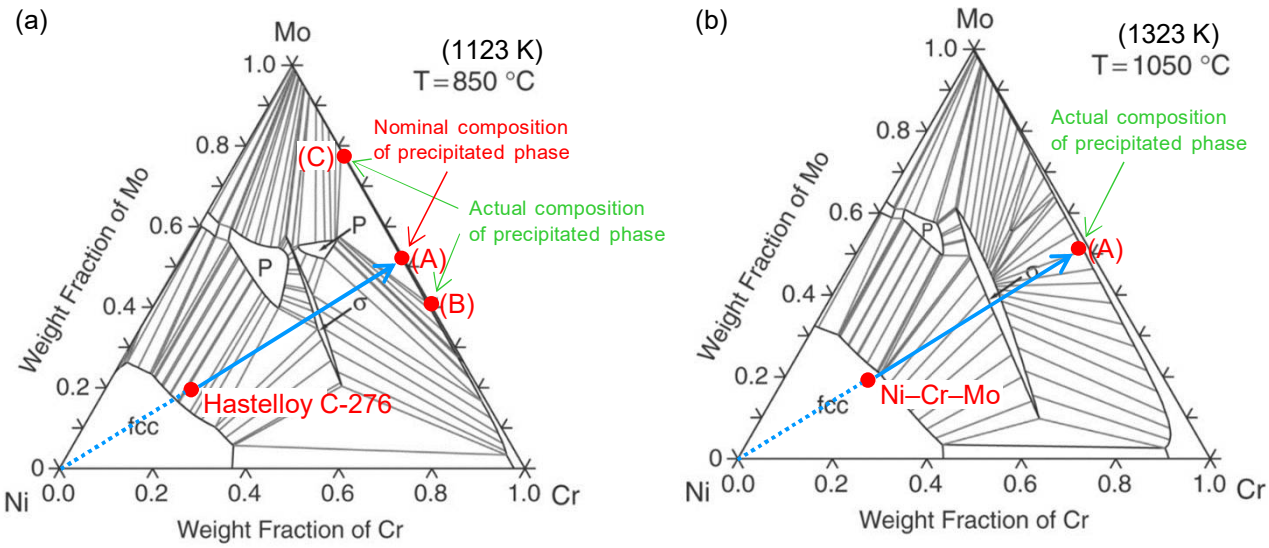

Fig. 7 Phase changes estimated using the evaluated isothermal sections of the Ni–Cr–Mo ternary phase diagram at (a) 1123 K and (b) 1323 K [33].

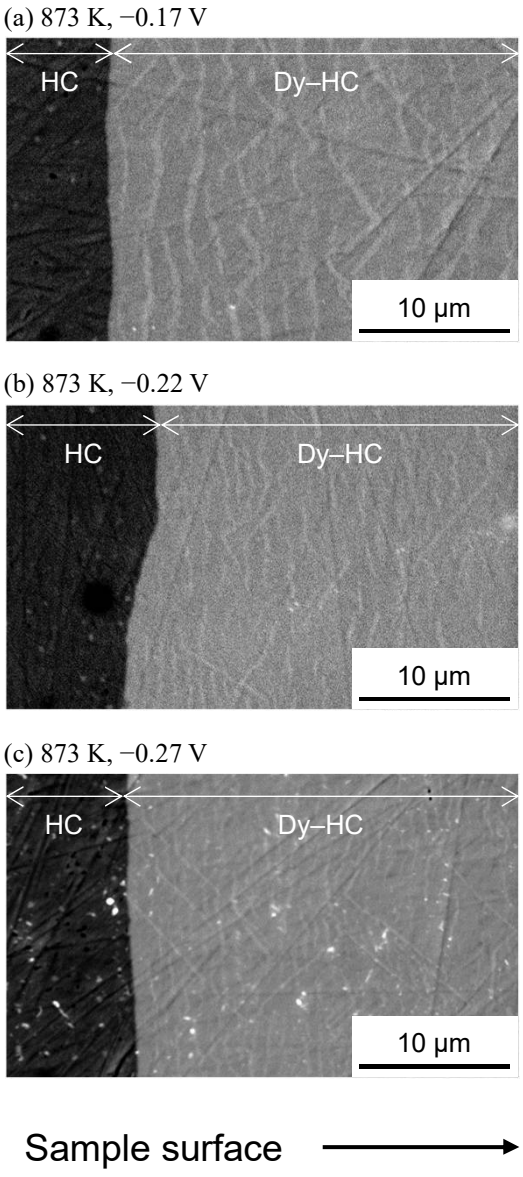

Fig. 8 Cross-sectional SEM images of samples obtained by potentiostatic electrolysis of HC plate electrodes at (a) −0.17 V, (b) −0.22 V, and (c) −0.27 V vs. E_{eq} ($DyNi_3/DyNi_2$) in molten LiCl–KCl–$DyCl_3$ (0.50 mol%) at 873 K. A charge density of 50 C cm^{-2} is used.

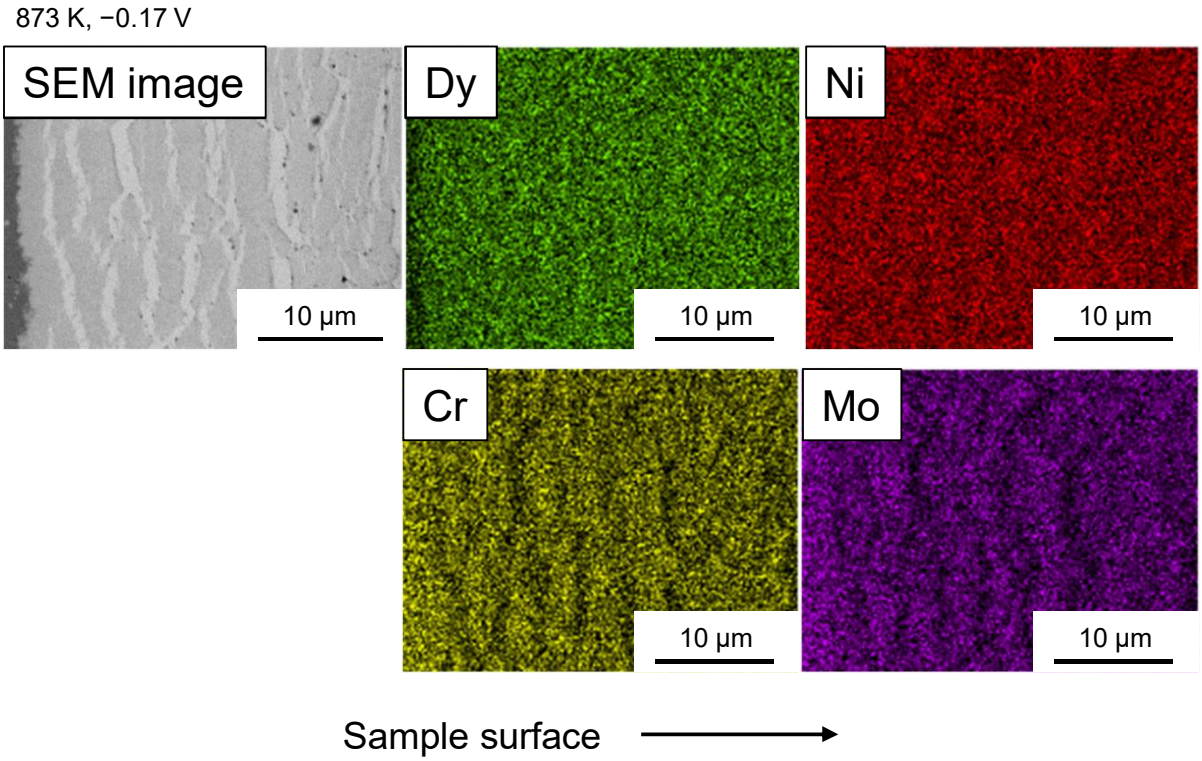

Fig. 9 Cross-sectional SEM and EDX mapping images of samples obtained by potentiostatic electrolysis of the HC plate electrode at −0.17 V vs. E_{eq} ($DyNi_3/DyNi_2$) for 260 min in molten LiCl–KCl–$DyCl_3$ (0.50 mol%) at 873 K. A charge density of 25 C cm^{-2} is used.

(a) Fluoride system at 1123–1323 K

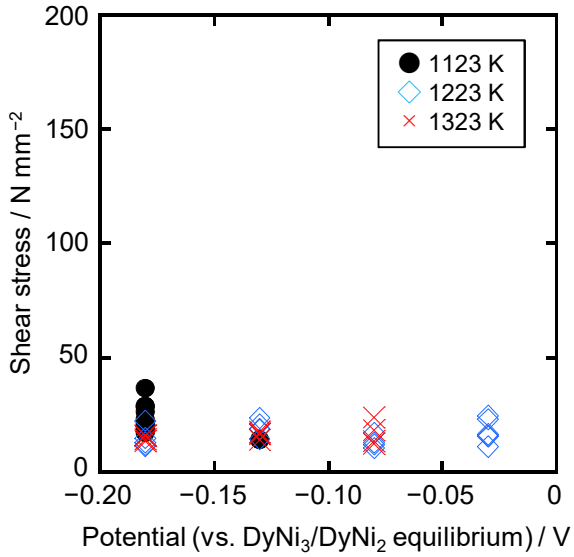

(b) Chloride system at 873 K

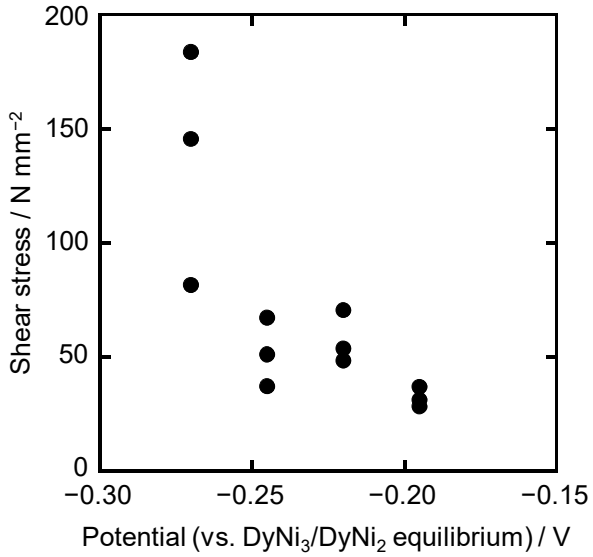

Fig. 10 Shear stress of samples prepared by potentiostatic electrolysis of HC plate electrodes in (a) molten LiF–CaF_2–DyF_3 (0.30 or 0.50 mol%) at 1123–1323 K and (b) molten LiCl–KCl–$DyCl_3$ (0.50 mol%) at 873 K.

(a) Fluoride system at 1323 K

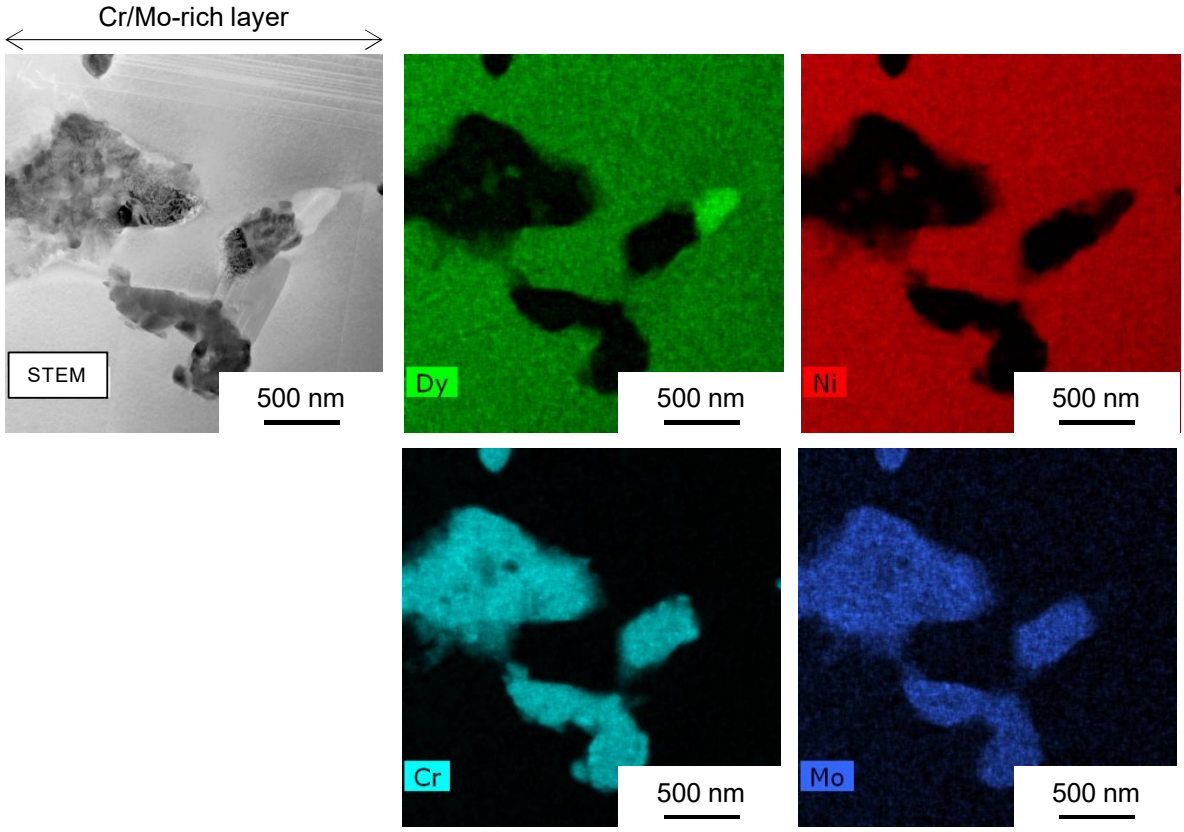

(b) Chloride system at 873 K

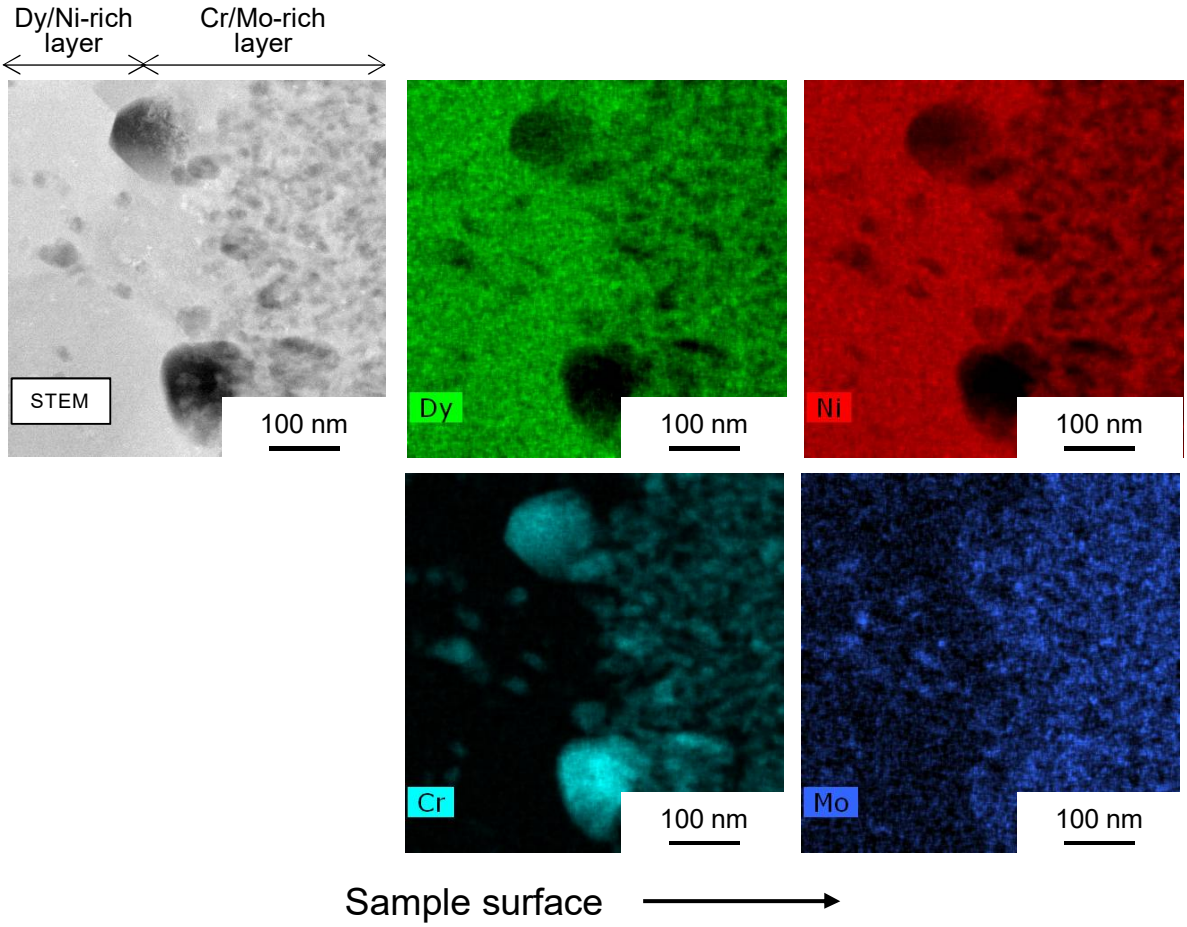

Fig. 11 High-angle annular dark field STEM images and EDX mapping images of samples obtained by potentiostatic electrolysis of HC plate electrodes at (a) −0.08 V vs. E_{eq} ($DyNi_3/DyNi_2$) for 30 min at 1323 K in molten LiF–CaF_2–DyF_3 (0.50 mol%) and (b) −0.17 V vs. E_{eq} ($DyNi_3/DyNi_2$) for 260 min in molten LiCl–KCl–$DyCl_3$ (0.50 mol%) at 873 K.